PCCP

PAPER

View Article Online
View Journal | View Issue

Cite this: *Phys. Chem. Chem. Phys.*, 2025, **27**, 9369

Metal–oxygen bonding characteristics dictate activity and stability differences of RuO_2 and IrO_2 in the acidic oxygen evolution reaction†

Longdan Tang,[ab] Xia Chen,[ab] Zhuoyang Xie,[ab] Qiong Xiang,[ab] Jin Liu,[ab] Li Li *[ab] and Zidong Wei [ab]

Received 19th February 2025,
Accepted 29th March 2025

DOI: 10.1039/d5cp00666j

rsc.li/pccp

Ruthenium dioxide (RuO_2) and iridium dioxide (IrO_2) serve as benchmark electrocatalysts for the acidic oxygen evolution reaction (OER), yet their intrinsic activity–stability relationships remain elusive. Herein, we employ density functional theory (DFT) calculations to systematically investigate the origin of divergent OER catalytic behaviors between RuO_2 and IrO_2 in acidic media. Mechanistic analyses reveal that RuO_2 follows the adsorbate evolution mechanism with superior activity (theoretical overpotential: 0.698 V *vs.* 0.909 V for IrO_2), while IrO_2 demonstrates enhanced stability due to a higher dissolution energy change (>2.9 eV *vs.* -0.306 eV for RuO_2). Electronic structure analysis reveals that RuO_2 exhibits ionic-dominated metal–oxygen bonds with delocalized electron distribution, facilitating intermediate desorption but promoting detrimental RuO_4^{2-} dissolution. In contrast, IrO_2 features covalent bonding characteristics with more electron filling in Ir–oxygen bonds (2.942 *vs.* 2.412 for RuO_2), thereby stabilizing surface intermediates against dissolution at the expense of higher OER barriers. This work establishes a clear correlation between the bonding nature and electrocatalytic performance metrics, offering fundamental insights for the rational design of acid-stable OER electrocatalysts with optimized activity–stability relationships.

1. Introduction

Electrochemical water splitting technology is widely regarded as an ideal method for utilizing renewable electricity to produce clean hydrogen (H_2) fuel.[1,2] Acidic proton exchange membrane water electrolyzers (PEMWEs), with outstanding proton conductivity, lower ohmic losses, and more compact system design, have been widely regarded as one of the most efficient technological devices for green hydrogen production, which has sparked extensive research interest.[3–5] However, the commercialization of PEMWEs is significantly hindered by the sluggish acidic oxygen evolution reaction (OER) kinetics, a bottleneck primarily attributed to the current lack of active, stable, and cost-effective OER catalysts.[6–10] To date, ruthenium (Ru)-based catalysts, particularly RuO_2, and iridium (Ir)-based catalysts, notably IrO_2, are commonly regarded as the preferred materials for anode catalysts due to their excellent durability and good activity in the commercial application of PEMWEs.[11–14]

Nevertheless, when it comes to large-scale applications, the two catalysts, RuO_2 and IrO_2, confront three pivotal constraints. Firstly, their scarcity and high cost pose a significant barrier, as the price of Ru can reach up to \$9523 per kg, and Ir can soar to \$60 670 per kg.[15,16] More importantly, Ru-based catalysts still grapple with formidable challenges in terms of long-term stability during the OER in acidic environments or PEM reactors.[10,17,18] Additionally, Ir exhibits a relatively high overpotential during the OER, resulting in lower energy efficiency.[14,19,20] These intertwined limitations collectively hinder the achievement of the Department of Energy's (DOE's) goal of reducing hydrogen production costs to below \$2 per kg by 2025.[21,22] In recent years, great efforts have been made to improve the Ru or Ir acidic OER performance *via* strategies such as multimetal oxides or doping (Mn-doped RuO_2,[23] Ta-RuO_2,[24] Hf-doped IrO_2,[25] and Re-doped IrO_2[26]), morphology and structure tuning (ultra-thin RuO_2 nanosheets,[27] single-atom Ru–N–C,[28] and Au@$AuIr_2$[20]), strain effect (Ru/RuO_2@NCS[29] and $Ta_{0.1}Tm_{0.1}Ir_{0.8}O_{2-\delta}$[14]), surface reconstruction ($CaCu_3Ru_4O_{12}$,[30] $A_2Ru_2O_7$, A = Y, Nd, Gd and Bi,[31] and $SrCo_{0.9}Ir_{0.1}O_{3-\delta}$[32]) and so on, resulting in enhanced OER activity and stability compared with commercial RuO_2 and IrO_2 nanoparticles in acids.

However, the longest lifetime achieved so far for these novel catalysts is only 2000 hours under electrochemical testing conditions for $Y_2Ru_{1.2}Ir_{0.5}O_7$.[33] This falls far short of meeting the needs of practical applications, especially when compared

---

[a] *State Key Laboratory of Advanced Chemical Power Sources (Chongqing University), Chongqing, 400044, China. E-mail: liliracial@cqu.edu.cn*

[b] *School of Chemistry and Chemical Engineering, Chongqing University, Chongqing, 400044, China*

† Electronic supplementary information (ESI) available. See DOI: https://doi.org/10.1039/d5cp00666j

to the target lifetime of 100 000–120 000 hours by 2050.[34] Conversely, studying and understanding the fundamental processes occurring in typical noble metal-based oxide catalysts (RuO_2 and IrO_2) is expected to have a high degree of universality and contribute to the development of low-cost and high-efficiency materials. Mechanistically, the reaction pathways of RuO_2 and IrO_2, especially the involvement of lattice oxygen, remain widely controversial. Macounova *et al.*[35] investigated the lattice oxygen participation of nanocrystalline RuO_2-based catalysts, revealing that lattice oxygen contributed roughly 9% in pure RuO_2 and even up to 50% in $Ru_{0.9}Ni_{0.1}O_2$. However, this finding was later challenged by a study that found no evidence of oxygen exchange occurring on any of the four orientation surfaces of RuO_2, regardless of whether the electrolyte is acidic or alkaline.[36] Similarly, researchers have also expressed differing views on the participation of lattice oxygen in IrO_2. Kasian *et al.*[37] considered the participation of lattice oxygen to be ubiquitous in the Ir-based oxide system, and the specific structural characteristics of the catalyst significantly influence the evolution pathway of lattice oxygen. Conversely, Scott *et al.*[38] concluded that lattice oxygen is, at most, a negligible contribution to the overall OER activity for Ir-based catalysts in acidic electrolytes. Furthermore, the specific dissolution path and dissolved products of RuO_2 and IrO_2, which will inevitably suffer corrosion due to the harsh acidic environment, have been widely concerned.[9,39–41] It is suggested that the over-oxidation of RuO_2, occurring at elevated temperatures and under high O_2 partial pressures or as a consequence of anodic polarization, leads to the production of volatile and water-soluble $RuO_4{}^{2-}$.[39,42] Alexandrov *et al.*[41] discovered the presence of two pivotal intermediates ($RuO_2(OH)$ and $RuO_2(OH)_2$) on the $RuO_2(110)$ surface, which couple the Ru dissolution process with the catalytic process at the atomic scale. Interestingly, it was computationally revealed that the dissolution of IrO_2 exhibits potential dependence, transforming into IrO_3 at high anodic potentials and into $Ir(OH)_3$ at low anodic potentials.[43] Nevertheless, other authors have experimentally discovered that IrO_2 ultimately dissolves in the form of $IrO_4{}^{2-}$ at high anodic potentials.[44] Evidently, the widespread controversies surrounding the catalytic activity and deactivation mechanisms of the two catalysts stem primarily from the lack of consensus in understanding their underlying mechanisms.

In our work, we explored the OER and the deactivation mechanisms of RuO_2 and IrO_2 in detail to understand the intrinsic differences in their activity and stability by density functional theory (DFT) calculations. Initially, we evaluated three distinct OER pathways for each catalyst to determine the thermodynamically favorable reaction routes. Subsequently, we analyzed potential deactivation mechanisms for both catalysts, with a focus on dissolution pathways, the species formed upon dissolution, and the resultant activity following the dissolution of active sites. Furthermore, we conducted a comprehensive assessment of their intrinsic electronic structures, examining orbital states and bonding characteristics, and correlated these elements with OER activity and stability. Our findings indicate that variations in metal–oxygen (M–O) bonding characteristics are the fundamental reason for the observed differences in performance. This research not only deepens our understanding of the differing performances between OER catalysts but also offers a robust theoretical framework to guide future optimization efforts in catalyst performance.

2. Computational details

Spin-polarized DFT calculations were conducted using the Vienna ab initio simulation package (VASP),[45,46] in which the ionic cores of all atoms are described by projector augmented wave (PAW) pseudopotentials.[47] The generalized gradient approximation (GGA) of the Perdew–Burke–Ernzerhof (PBE)[48] exchange-functional was applied, along with D3-dispersion correction (BJ)[49,50] to account for long-range van der Waals interactions. During the optimization of geometric structures using a force-based conjugate gradient method, the convergence thresholds for force and energy were set to 0.02 eV $Å^{-1}$ and 10^{-5} eV, respectively. The cut-off energy for plane-wave basis was set as 450 eV.

The lattice parameters of the rutile structure were optimized to give a = 4.490 Å, c = 3.118 Å for RuO_2, and a = 4.527 Å, c = 3.173 Å for IrO_2, which is in agreement with a previous experimental prediction.[51] The Brillouin zone was sampled using the Monkhorst–Pack scheme with a 6 × 6 × 8 k-point mesh for RuO_2 and IrO_2 cells. Detailed information regarding the optimized structure of the cell model is provided in Fig. S1 and Tables S1, S2 (ESI†). In our calculations, we selected the $MO_2(110)$ (M = Ru, Ir) surfaces, the most stable structure that have been extensively studied.[36,38,41,43,52–54] It is noteworthy that the rutile (110) surface comprises two distinct metal positions: a coordinatively unsaturated site (Cus) that is not capped by oxygen and is bound to five O atoms, and a bridge site (Bri) that is bound to six O atoms. We utilized the slab model consisting of 48 M atoms and 96 O atoms, where the first layer was fixed during geometry optimization, as depicted in Fig. 1. Tables S1 and S2 (ESI†) present the relevant parameters of the optimized geometric structures of $RuO_2(110)$ and $IrO_2(110)$. In subsequent discussions, we will uniformly adopt RuO_2 and IrO_2 to refer to the corresponding surface materials, respectively. For the calculations of the slab, the k-point mesh was set to 3 × 3 × 1. A 20 Å thick vacuum layer was introduced perpendicular to the surface to minimize any potential interactions between periodic replicas. Due to the strong correlation of d electrons in Ru and Ir, a $U–J$ value of 2.0 eV was adopted and spin polarization was considered in our study.[55,56] More details regarding the calculation formulas and derivation process can be found in the ESI.†

3. Results and discussion

3.1 OER mechanism and activity of RuO_2 and IrO_2

Three general mechanisms of OER in an acid medium, including the adsorbate evolution mechanism (AEM), lattice oxygen oxidation mechanism (LOM), and oxidation pathway mechanism (OPM), are described in Fig. 2a–c.[57–60] In the complete

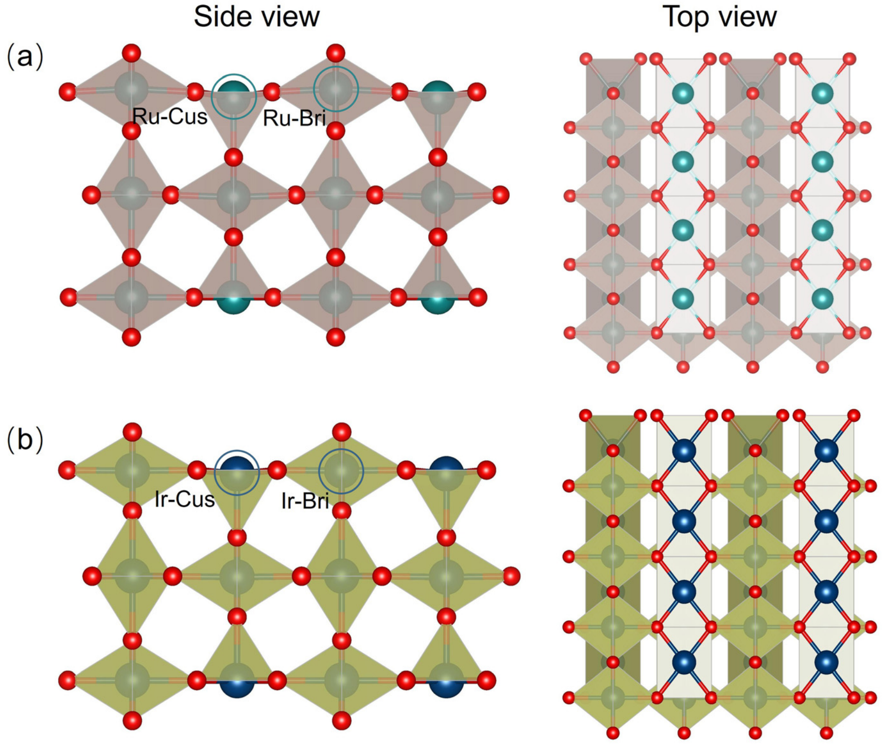

Fig. 1 Side view and top view of (a) RuO_2(110) and (b) IrO_2(110). Ru–Cus and Ir–Cus denote the active sites. Color code: dark green balls are Ru atoms, dark blue balls denote Ir atoms, and red balls represent O atoms.

crystalline structure, we select the Cus site as the active site (Fig. S2, ESI†). When defects occur, the Bri site is also exposed to a five-coordinate environment and serves as the active site (Fig. S3, ESI†). For traditional AEM, water firstly deprotonates to a hydroxyl anion (OH^-), oxidized to an *OH intermediate that adsorbs on the active site (M). Afterward, the *OH deprotonates generate an *O intermediate, which is subsequently attacked by OH^- yielding an *OOH intermediate. Finally, The O_2 dissociates from the catalyst surface *via* deprotonation, freeing up the active site and enabling the continuation of the reaction cycle. For the LOM, while the initial two steps closely resemble the AEM, divergence emerges from the third step where *O interacts with lattice oxygen to produce O_2, leaving an oxygen vacancy site (O_V). Subsequently, the vacancy is occupied by *OH, which ultimately undergoes deprotonation to drive the reaction cycle forward. Different from the single-site mechanism of the AEM and LOM, OPM demonstrates a dual-site mechanism. After an *OH intermediate is generated at a metal site, a water molecule, acting as a nucleophile, attacks the adjacent active site once again, leading to the formation of *OH adsorption at that location, thereby achieving a dual-site-adsorbed *OH state (*OH_*OH). Subsequently, dehydrogenation reactions occur sequentially at the two adsorption sites, first transitioning into an *OH_*O structure and then into an *O_*O structure, ultimately culminating in O_2 production and the perpetuation of the reaction cycle.

The reaction thermodynamics for these three mechanisms on the bare RuO_2 and IrO_2 facets are compared. The free energy diagrams for the OER *via* the AEM, LOM, and OPM on the RuO_2 and IrO_2 surfaces are respectively presented in Fig. 2d. For the AEM, forming *OH and *O on RuO_2 is inherently spontaneous, while generating *OOH and O_2 poses relatively more challenges. Specifically, the transition from *OOH to O_2 generation serves as the potential-determining step (PDS). A similar trend is observed for IrO_2, consistent with a previous result.[61] Under the thermodynamic equilibrium potential of 1.23 V (*vs.* RHE), the theoretical OER overpotential (η) of RuO_2 is 0.698 V, significantly lower than that of IrO_2, which is 0.909 V. This demonstrates that RuO_2 has higher activity and a distinct advantage over IrO_2 from a thermodynamic perspective. It is attributed to the fact that the single active site of RuO_2 shows a weaker interaction with *OOH than IrO_2. Moreover, the reaction trends of both catalysts following the AEM mechanism exhibited nearly identical behaviour under both solvation and vacuum conditions (Fig. S4, ESI†). This consistency strongly supports the conclusion that solvation effects play a minimal role in the catalytic system under study.

In the case of LOM, the difficulty in forming oxygen vacancies (Table S3, ESI†) poses a significant challenge for the production of O_2, resulting in an exceptionally high theoretical overpotential, which ultimately hinders both oxides from effectively undergoing this mechanism. For the OPM featuring dual active sites, when the phenomenon of dual-site adsorption is observed, it is found that the species adsorption is too strong on both RuO_2 and IrO_2, resulting in significant difficulties in the desorption process. Therefore, the OPM is not applicable. Fig. 2e compares the theoretical overpotential to the AEM, LOM, and OPM pathways on RuO_2 and IrO_2, respectively.

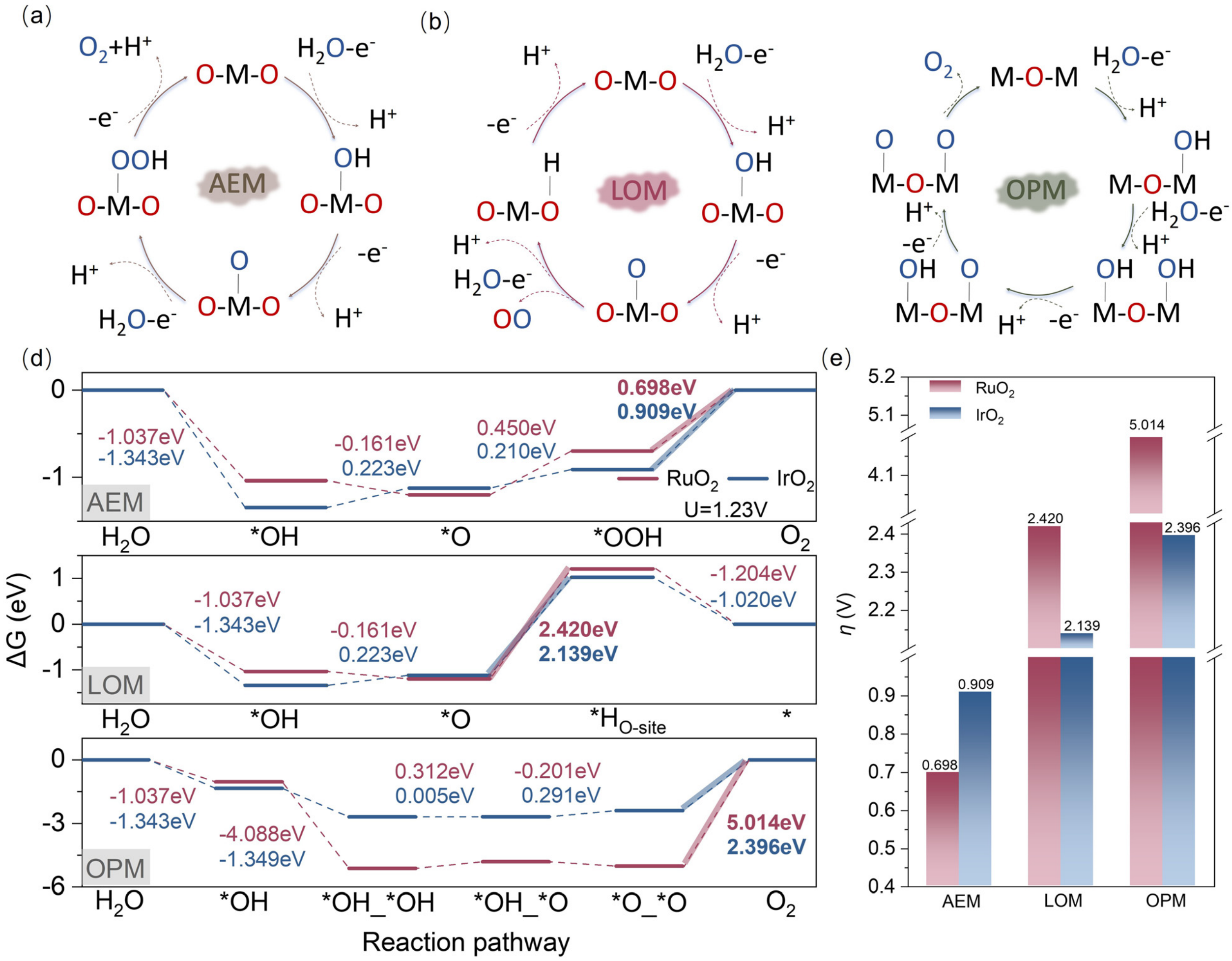

Fig. 2 (a)–(c) Schematic representations of three OER pathways (a) AEM (b) LOM (c) OPM on the surface of RuO_2 and IrO_2 considered in this study. Red oxygen and blue oxygen represent lattice oxygen and oxygen from an acidic environment, respectively. M stands for metal (Ru, Ir). (d) Gibbs free energy diagrams for the AEM, LOM, and OPM for the OER at 1.23 V on RuO_2 and IrO_2. The thick lines in the figures represent PDS. (e) Overpotential for different reaction pathways for RuO_2 and IrO_2.

The results suggest that the OER on the RuO_2 and IrO_2 is thermodynamically more likely to follow the AEM rather than the LOM or OPM, in good agreement with previous investigations.[51,62,63]

3.2 The OER deactivation mechanism of RuO_2 and IrO_2

Fig. 3a illustrates the potential deactivation pathways during the OER process. The LOM pathway is less likely to occur due to the inherent presence of vacancies, while the oxygen-containing intermediates in both AEM and OPM may disrupt the structure of active sites, leading to dissolution. For instance, the adsorption of intermediates like *OH and *O combined with lattice oxygen results in the leaching of MO_3 from the active site and the formation of tetra-coordinated MO_4^{2-} through further oxidation of MO_3 by the electrolyte. When *OOH adsorbed, or a dual-site adsorption phenomenon occurs (*i.e.*, the adsorbed species are *OH_*OH, *OH_*O, or *O_*O), the dissolution of tetra-coordinated MO_4^{2-} can be triggered directly.

The dissolution of active sites is closely related to the stability of the RuO_2 and IrO_2 structures and their defect configurations after dissolution. The thermodynamic stability of the defect configurations after the dissolution of catalysts has been thoroughly evaluated, as shown in Fig. S5 and S6 (ESI†). Table S4 (ESI†) presents the formation energies for all defect configurations. A smaller formation energy indicates a more stable defect structure, making it more likely to occur during dissolution. In the case of RuO_2, defect configuration 6 is the most stable, formed by releasing a five-coordinated Ru and two neighbouring bridge O atoms. On the other hand, for IrO_2, defect configuration 4 is the most stable and is more readily formed by the interaction of a six-coordinated Ir atom with two neighbouring bridge O atoms.

Fig. 3b and Fig. S7 (ESI†) show that the dissolution of the Ru site in RuO_2 mainly produces the four-coordinate RuO_4^{2-} species rather than the three-coordinate RuO_3 species, being more thermodynamically favoured in the AEM, with distinct negative free energy changes. In comparison, the dissolution of RuO_3 requires an uphill free energy of over 1.5 eV. Specifically, all the intermediates in the AEM can spontaneously induce the dissolution of the Ru sites into the RuO_4^{2-}. As the valence state of the Ru site increases, the more negative free energy changes

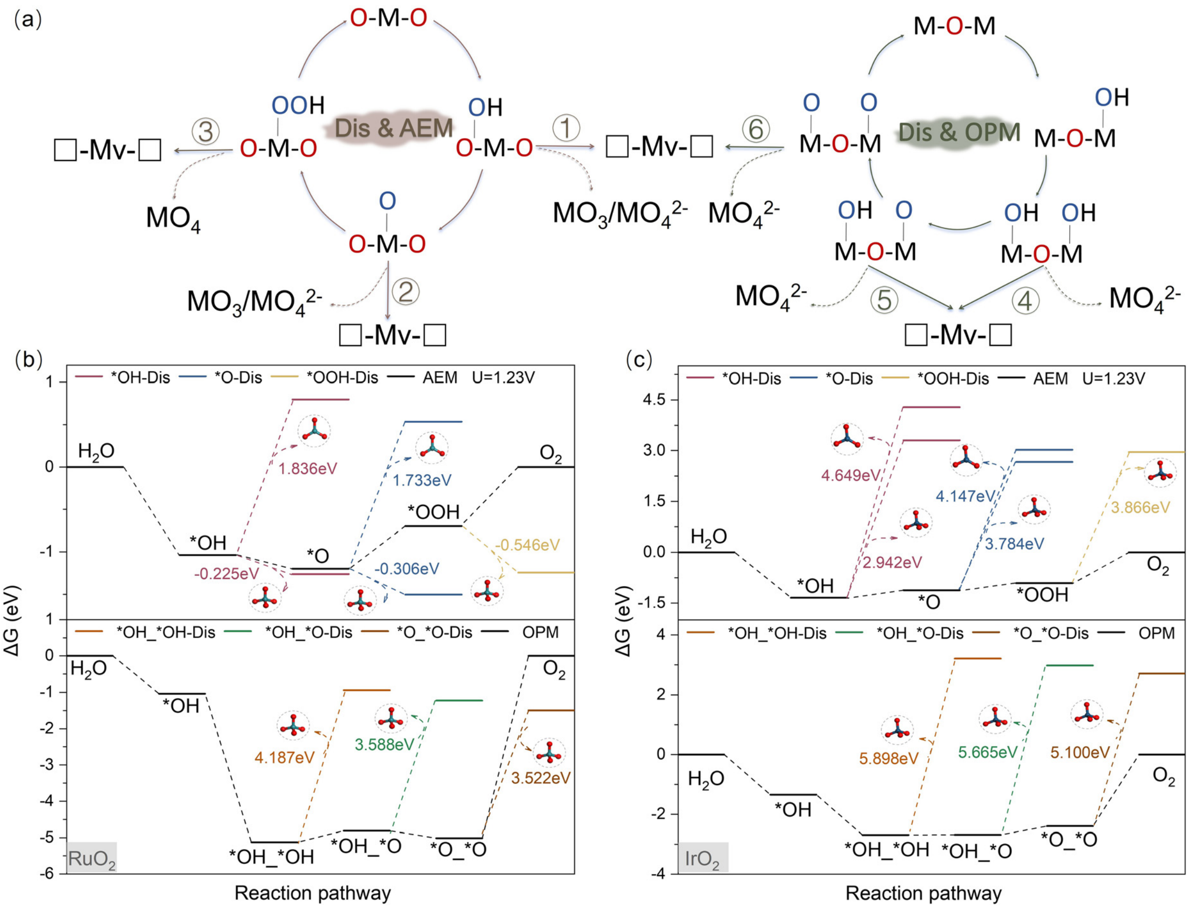

Fig. 3 (a) Schematic representations of the dissolution pathways on the surface of RuO_2 and IrO_2. Red oxygen and blue oxygen represent lattice oxygen and oxygen from the solution, respectively. M stands for metal (Ru, Ir). Mv and square represent the formation of metal vacancies and oxygen vacancies, respectively. (b) Dissolution-free energy diagram of AEM and OPM coupling with corrosion for RuO_2 at 1.23 V. (c) Dissolution-free energy diagram of AEM and OPM coupling with corrosion for IrO_2 at 1.23 V.

become, indicating the easier dissolution of active sites. During the OPM, the dissolution pathway of RuO_2 is non-spontaneous, with a free energy requirement for the leaching of RuO_4^{2-} exceeding 3.5 eV. These findings indicate that RuO_2 has a strong tendency to dissolve in the AEM of the OER. Regarding the dissolution behaviour of RuO_2 catalysts, the influence of solvation effects has been further investigated. By coupling the dissolution process with AEM, the dissolution pathway and trend show excellent agreement with the results obtained under vacuum conditions (Fig. S9, ESI†). This finding indicates that solvation effects have negligible impact on the dissolution behaviour of RuO_2 catalysts in our studied system. In addition, once the Ru defects formed on the RuO_2, as illustrated in Fig. S10 (ESI†), the theoretical overpotential for the OER increases to over 1.5 V, showing a significant depression in OER intrinsic activity. It means that the dissolution of the Ru site during OER catalysis is the main reason for the deactivation of the RuO_2 catalyst. Preserving the integrity of the crystal structure of RuO_2 as much as possible is an effective strategy to maintain its high intrinsic OER activity.

In comparison to RuO_2, the dissolution pathways of IrO_2 during AEM and OPM, as shown in Fig. 3c, are thermodynamically non-spontaneous. The free energy changes of the dissolution step, whether dissolved as IrO_4^{2-} or IrO_3, are higher than 2.9 eV, indicating considerable thermodynamic non-feasible. This highlights the remarkable stability of IrO_2 throughout the entire OER process. Interestingly, once IrO_2 has a defect, it exhibits enhanced intrinsic activity in both AEM and OPM compared to the IrO_2 surface (Fig. S10, ESI†). This indicates that pre-introducing oxygen vacancies in the IrO_2 surface is an effective way to improve the OER activity of IrO_2. Upon comparing the dissolution performance of IrO_2 and RuO_2, it is evident that IrO_2 exhibits higher stability during the OER process.

3.3 The descriptor of activity and stability for the OER

An investigation of the electronic structure reveals that the bonding properties of RuO_2 and IrO_2 are attributed to the contrasting trends in their activity and stability. Fig. 4a displays the projected density of states (PDOS), illustrating the overlap of the orbitals from metal and oxygen atoms and how electrons are distributed in both compounds. Notably, the energy level of the bonding orbitals in IrO_2 is lower than that in RuO_2, whereas the energy level of the antibonding orbitals is higher in IrO_2. This observation indicates that the overlap of the Ir-d orbitals with the O-p orbitals is more significant than that of the Ru-d orbitals with the O-p orbitals, suggesting that the Ir–O bonding has a greater covalency than Ru–O bonding. Further confirmation comes from the projected crystal orbital Hamilton overlap population (pCOHP) analysis, which shows that the electron filling in the Ir–O bonds (2.942) is notably higher than in RuO_2 (2.412), indicating stronger covalency in the Ir–O bond. Additionally, the energy difference between the d-band of Ru and the p-band of O ($\varepsilon_d - \varepsilon_p$) is smaller for RuO_2 (1.328 eV) compared to IrO_2 (1.456 eV), indicating more ionic bonding nature in the Ru–O bond. This is also supported by the electronic localization function (ELF) analysis, which reveals that the Ru–O bonds exhibit a lower electronic delocalization value (0.475). In contrast, the Ir–O bonds have a higher value (0.511), suggesting a more covalency bonding nature due to increased electronic localization.[64,65] Furthermore, the electronic distributions of RuO_2–V and IrO_2–V exhibit significant changes after vacancy formation (Fig. S11, ESI†). For RuO_2–V, ε_d shifts positively, and ε_p shifts negatively, resulting in an increase in $\varepsilon_d - \varepsilon_p$. In contrast, for IrO_2–V, ε_d shifts negatively and ε_p shifts positively, leading to a decrease in $\varepsilon_d - \varepsilon_p$, showing an opposite trend. Analysis of the pCOHP of the defective catalysts reveals that the bonding orbital interaction of RuO_2–V (−ICOHP = 2.723) is enhanced compared to the intact catalyst, while that of IrO_2–V (−ICOHP = 2.911) is weakened. Therefore, it can be concluded that the nature of the metal–oxygen bonds may have changed after defect formation, leading to the observed changes in catalytic activity.

The covalent Ir–O bonds contribute to the stability of IrO_2, even after the adsorption of OER intermediates. However, these bonds with more localized electrons also impede the release of O_2 by enhancing the adsorption strength of the intermediates. In contrast, the greater ionic bonding characteristics of RuO_2 with more delocalized electrons facilitate O_2 formation and desorption; nonetheless, the Ru–O structure is more susceptible to disruption by the adsorption of intermediates. Fig. 4b illustrates significant variations in the charge transfer number (δQ_M) associated with active sites upon the adsorption of three intermediate species: *O, *OH, and *OOH. During this adsorption process, the metal active sites of the oxides interact with the intermediates primarily through covalent interaction (orbital overlap) and electrostatic interactions. A higher degree of orbital overlap correlates with increased charge transfer and enhanced binding strength. In RuO_2, its greater ionic bonding

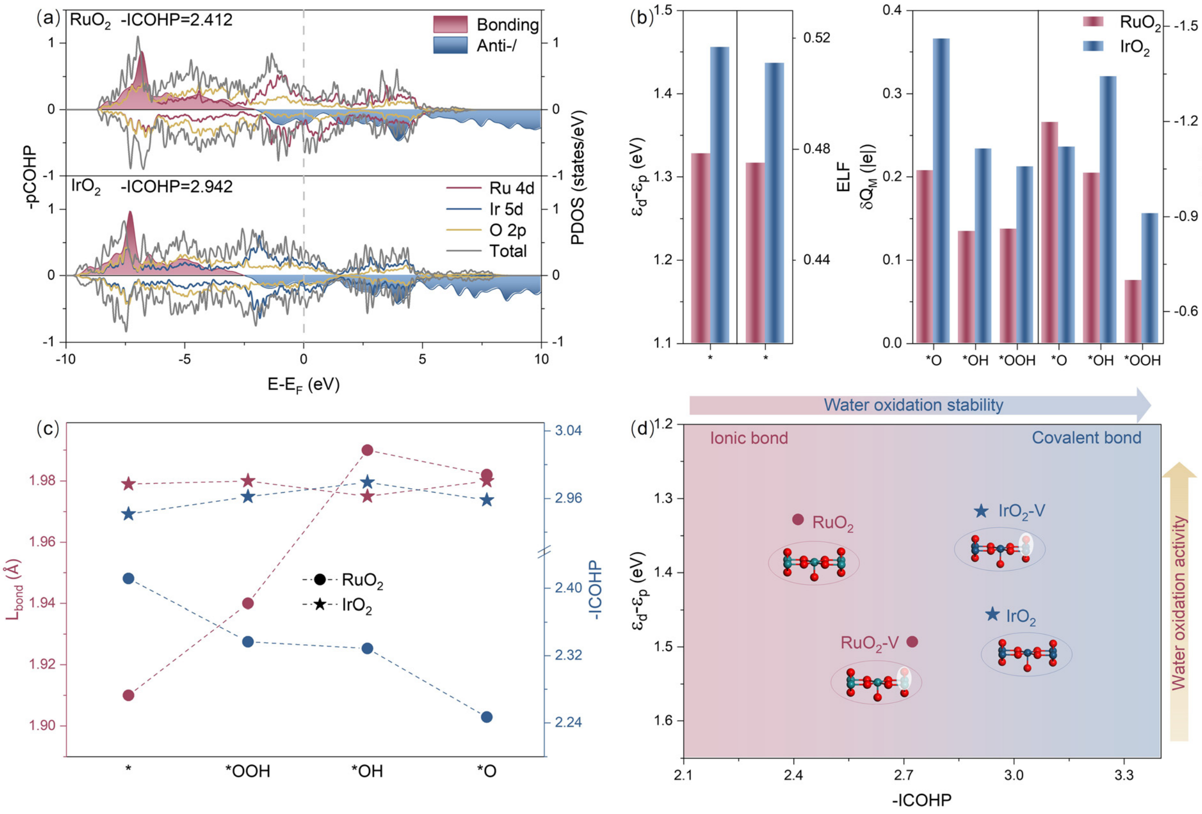

Fig. 4 (a) Projected crystal orbital Hamilton overlap population (pCOHP) curves and projected density of states (PDOS) plots of M-d and O-p in the RuO_2 and IrO_2 models. The dashed line refers to the Fermi level. (b) Values of the difference between d-band and p-band centers ($\varepsilon_d - \varepsilon_p$) and electronic localization function (ELF) for RuO_2 and IrO_2; changes in charge transfer numbers (δQM) on the metal active after the adsorption of intermediates on RuO_2 and IrO_2; changes in Gibbs free energy of AEM (Δ*G*) at 1.23 V on RuO_2 and IrO_2. (c) Correlation between the calculated bond lengths between the bulk metal and oxygen, and −ICOHP of the bulk after the adsorption of intermediates on RuO_2 and IrO_2. (d) The regular trends of $\varepsilon_d - \varepsilon_p$ and −ICOHP with respect to the water oxidation activity and stability. RuO_2 and IrO_2 represent the pristine (110) crystal surfaces, while RuO_2–V and IrO_2–V represent the defective crystal surfaces.

leads to the adsorption of intermediate species mainly through electrostatic interactions, resulting in lower electron transfer and relatively weaker binding. In contrast, the covalent bonding nature of IrO_2 promotes stronger overlap between the Ir orbitals and those of the intermediate species, leading to more significant electron transfer and stronger adsorption.

As shown in Fig. 4c, while the Ir–O bond length in IrO_2 (1.979 Å) is notably longer than the Ru–O bond length in RuO_2 (1.910 Å) due to the larger radius of Ir, the Ru–O bond length of RuO_2 significantly elongates upon the adsorption of reaction intermediates, whereas that of IrO_2 remains largely unchanged. This geometric behavior highlights the tendency of RuO_2 to undergo deformation, indicating its lower stability. Furthermore, the −ICOHP value for RuO_2 decreases considerably, while that of IrO_2 remains relatively stable (Fig. S12, ESI†).

Fig. 4d illustrates the complex relationship between the bonding properties of RuO_2 and IrO_2 and their catalytic performance. It demonstrates that electron filling in the M–O bonds contributes to the stability of these oxides. Specifically, a higher degree of electron filling in the M–O bonds makes the catalyst less susceptible to external disturbances, as evidenced by the highly stable IrO_2. In contrast, the difference between ε_d and ε_p in an oxide can indicate its OER activity. Smaller $\varepsilon_d - \varepsilon_p$ values correlate with more delocalized electrons and weaker adsorption of intermediates at reactive sites, which is favorable for the release of oxygen. RuO_2 serves as a prime example of a catalyst with excellent OER activity. To enhance the stability of RuO_2, it is essential to increase the electron filling degree in Ru–O bonds to maintain structural integrity. This can be achieved by doping electron-rich atoms, as demonstrated by Zhang *et al.*,[66] where La doping in RuO_2 forms a La–O–Ru local structure, optimizes Ru–O bond strength, enhances RuO_2 stability, and suppresses Ru dissolution, enabling stable operation for 450 hours at 100 mA cm^{-2}. On the other hand, improving IrO_2 activity requires increasing the delocalized electrons on Ir, which can be realized by either reducing Ir–O orbital overlap or introducing oxygen vacancies. Wang *et al.*[67] exemplified this approach through their Gd-doped IrO_2 catalyst, synthesized *via* template-free ammonia complexation. The Gd doping optimized OER performance by regulating the Ir^{4+}/Ir^{3+} ratio and increasing oxygen vacancy concentration, leading to enhanced H_2O adsorption and reduced *OH dissociation energy.

4. Conclusions

Our comprehensive thermodynamic analysis reveals the dominant reaction pathways governing both OER mechanisms and dissolution processes in RuO_2 and IrO_2 catalysts. The AEM emerges as the predominant OER pathway for both oxides, with RuO_2 demonstrating superior catalytic activity compared to IrO_2. Crucially, this AEM pathway drives the thermodynamically spontaneous dissolution of RuO_2 into soluble RuO_4^{2-} species, while maintaining IrO_2's exceptional stability through non-spontaneous dissolution characteristics. Electronic structure analysis through $\varepsilon_d - \varepsilon_p$ energy gaps, ELF, and −ICOHP values uncovers fundamental bonding differences: RuO_2 exhibits ionic-dominated bonding with significant electron delocalization, whereas IrO_2 displays covalent-dominated interactions with higher electron filling. This contrast creates an intrinsic activity–stability trade-off; the ionic character in RuO_2 weakens intermediate adsorption to enhance OER activity but sacrifices structural integrity through labile metal–oxygen bonds. Conversely, IrO_2's covalent nature stabilizes the catalyst framework but strengthens intermediate binding, thereby limiting catalytic performance.

These atomistic insights establish a fundamental structure–activity–stability relationship. The revealed electronic origins of the RuO_2 and IrO_2 difference provide critical design principles for next-generation OER catalysts: strategic engineering of metal–oxygen bonding character through alloying, strain modulation, or heterostructure construction could potentially decouple the activity–stability correlation, enabling simultaneous optimization of both essential properties for practical water electrolysis applications.

Author contributions

L. T. performed the theoretical calculations and the interpretation. L. T., X. C. and Z. X. were responsible for data collection and analysis. L. L. and L. T. conducted the data analysis and wrote this manuscript. Q. X. and J. L. contributed to the revision. L. L. and Z. W. directed the project and finalized the manuscript. All authors discussed the results and contributed to the final manuscript.

Data availability

The data supporting the findings of this study are available within the article and its ESI.†

Conflicts of interest

There are no conflicts to declare.

Acknowledgements

This work was supported by the National Key Research and Development Program of China (2021YFB4000300) and the National Natural Science Foundation of China (21822803).

References

1 J. A. Turner, Sustainable Hydrogen Production, *Science*, 2004, **305**, 972–974.

2 I. Dincer and M. I. Aydin, New paradigms in sustainable energy systems with hydrogen, *Energy Convers. Manage.*, 2023, **283**, 116950.

3 M. Carmo, D. L. Fritz, J. Mergel and D. Stolten, A comprehensive review on PEM water electrolysis, *Int. J. Hydrogen Energy*, 2013, **38**, 4901–4934.

4 C. Spöri, J. T. H. Kwan, A. Bonakdarpour, D. P. Wilkinson and P. Strasser, The Stability Challenges of Oxygen Evolving Catalysts Towards a Common Fundamental Understanding and Mitigation of Catalyst Degradation, *Angew. Chem., Int. Ed.*, 2017, **56**, 5994–6021.

5 S. Pan, H. Li, D. Liu, R. Huang, X. Pan, D. Ren, J. Li, M. Shakouri, Q. Zhang, M. Wang, C. Wei, L. Mai, B. Zhang, Y. Zhao, Z. Wang, M. Graetzel and X. Zhang, Efficient and stable noble-metal-free catalyst for acidic water oxidation, *Nat. Commun.*, 2022, **13**, 2294.

6 J. Song, C. Wei, Z.-F. Huang, C. Liu, L. Zeng, X. Wang and Z. J. Xu, A review on fundamentals for designing oxygen evolution electrocatalysts, *Chem. Soc. Rev.*, 2020, **49**, 2196–2214.

7 Q. Wang, X. Huang, Z. L. Zhao, M. Wang, B. Xiang, J. Li, Z. Feng, H. Xu and M. Gu, Ultrahigh-Loading of Ir Single Atoms on NiO Matrix to Dramatically Enhance Oxygen Evolution Reaction, *J. Am. Chem. Soc.*, 2020, **142**, 7425–7433.

8 Y.-R. Zheng, J. Vernieres, Z. Wang, K. Zhang, D. Hochfilzer, K. Krempl, T.-W. Liao, F. Presel, T. Altantzis, J. Fatermans, S. B. Scott, N. M. Secher, C. Moon, P. Liu, S. Bals, S. Van Aert, A. Cao, M. Anand, J. K. Nørskov, J. Kibsgaard and I. Chorkendorff, Monitoring oxygen production on mass-selected iridium–tantalum oxide electrocatalysts, *Nat. Energy*, 2021, **7**, 55–64.

9 L. An, C. Wei, M. Lu, H. Liu, Y. Chen, G. G. Scherer, A. C. Fisher, P. Xi, Z. J. Xu and C. Yan, Recent Development of Oxygen Evolution Electrocatalysts in Acidic Environment, *Adv. Mater.*, 2021, **33**, 2006328.

10 Y. Wen, P. Chen, L. Wang, S. Li, Z. Wang, J. Abed, X. Mao, Y. Min, C. T. Dinh, P. D. Luna, R. Huang, L. Zhang, L. Wang, L. Wang, R. J. Nielsen, H. Li, T. Zhuang, C. Ke, O. Voznyy, Y. Hu, Y. Li, W. A. Goddard III, B. Zhang, H. Peng and E. H. Sargent, Stabilizing Highly Active Ru Sites by Suppressing Lattice Oxygen Participation in Acidic Water Oxidation, *J. Am. Chem. Soc.*, 2021, **143**, 6482–6490.

11 L. An, F. Yang, C. Fu, X. Cai, S. Shen, G. Xia, J. Li, Y. Du, L. Luo and J. Zhang, A Functionally Stable RuMn Electrocatalyst for Oxygen Evolution Reaction in Acid, *Adv. Funct. Mater.*, 2022, **32**, 2200131.

12 K. Wang, Y. Wang, B. Yang, Z. Li, X. Qin, Q. Zhang, L. Lei, M. Qiu, G. Wu and Y. Hou, Highly active ruthenium sites stabilized by modulating electron-feeding for sustainable acidic oxygen-evolution electrocatalysis, *Energy Environ. Sci.*, 2022, **15**, 2356–2365.

13 Q. Shi, C. Zhu, D. Du and Y. Lin, Robust noble metal-based electrocatalysts for oxygen evolution reaction, *Chem. Soc. Rev.*, 2019, **48**, 3181–3192.

14 S. Hao, H. Sheng, M. Liu, J. Huang, G. Zheng, F. Zhang, X. Liu, Z. Su, J. Hu, Y. Qian, L. Zhou, Y. He, B. Song, L. Lei, X. Zhang and S. Jin, Torsion strained iridium oxide for efficient acidic water oxidation in proton exchange membrane electrolyzers, *Nat. Nanotechnol.*, 2021, **16**, 1371–1377.

15 Z. Shi, J. Li, Y. Wang, S. Liu, J. Zhu, J. Yang, X. Wang, J. Ni, Z. Jiang, L. Zhang, Y. Wang, C. Liu, W. Xing and J. Ge, Customized reaction route for ruthenium oxide towards stabilized water oxidation in high-performance PEM electrolyzers, *Nat. Commun.*, 2023, **14**, 843.

16 D. A. Kuznetsov, M. A. Naeem, P. V. Kumar, P. M. Abdala, A. Fedorov and C. R. Müller, Tailoring Lattice Oxygen Binding in Ruthenium Pyrochlores to Enhance Oxygen Evolution Activity, *J. Am. Chem. Soc.*, 2020, **142**, 7883–7888.

17 Y. Yao, S. Hu, W. Chen, Z.-Q. Huang, W. Wei, T. Yao, R. Liu, K. Zang, X. Wang, G. Wu, W. Yuan, T. Yuan, B. Zhu, W. Liu, Z. Li, D. He, Z. Xue, Y. Wang, X. Zheng, J. Dong, C.-R. Chang, Y. Chen, X. Hong, J. Luo, S. Wei, W.-X. Li, P. Strasser, Y. Wu and Y. Li, Engineering the electronic structure of single atom Ru sites via compressive strain boosts acidic water oxidation electrocatalysis, *Nat. Catal.*, 2019, **2**, 304–313.

18 S. Hao, M. Liu, J. Pan, X. Liu, X. Tan, N. Xu, Y. He, L. Lei and X. Zhang, Dopants fixation of Ruthenium for boosting acidic oxygen evolution stability and activity, *Nat. Commun.*, 2020, **11**, 5368.

19 S. Cherevko, S. Geiger, O. Kasian, N. Kulyk, J.-P. Grote, A. Savan, B. R. Shrestha, S. Merzlikin, B. Breitbach, A. Ludwig and K. J. J. Mayrhofer, Oxygen and hydrogen evolution reactions on Ru, RuO_2, Ir, and IrO_2 thin film electrodes in acidic and alkaline electrolytes: A comparative study on activity and stability, *Catal. Today*, 2016, **262**, 170–180.

20 H. Wang, Z. Chen, D. Wu, M. Cao, F. Sun, H. Zhang, H. You, W. Zhuang and R. Cao, Significantly Enhanced Overall Water Splitting Performance by Partial Oxidation of Ir through Au Modification in Core–Shell Alloy Structure, *J. Am. Chem. Soc.*, 2021, **143**, 4639–4645.

21 H. Over, Fundamental Studies of Planar Single-Crystalline Oxide Model Electrodes (RuO_2, IrO_2) for Acidic Water Splitting, *ACS Catal.*, 2021, **11**, 8848–8871.

22 J. Yu, Q. He, G. Yang, W. Zhou, Z. Shao and M. Ni, Recent Advances and Prospective in Ruthenium-Based Materials for Electrochemical Water Splitting, *ACS Catal.*, 2019, **9**, 9973–10011.

23 S. Chen, H. Huang, P. Jiang, K. Yang, J. Diao, S. Gong, S. Liu, M. Huang, H. Wang and Q. Chen, Mn-Doped RuO_2 Nanocrystals as Highly Active Electrocatalysts for Enhanced Oxygen Evolution in Acidic Media, *ACS Catal.*, 2020, **10**, 1152–1160.

24 J. Zhang, X. Fu, S. Kwon, K. Chen, X. Liu, J. Yang, H. Sun, Y. Wang, T. Uchiyama, Y. Uchimoto, S. Li, Y. Li, X. Fan, G. Chen, F. Xia, J. Wu, Y. Li, Q. Yue, L. Qiao, D. Su, H. Zhou, W. A. Goddard and Y. Kang, Tantalum-stabilized ruthenium oxide electrocatalysts for industrial water electrolysis, *Science*, 2025, **387**, 48–55.

25 F. Zhao, B. Wen, W. Niu, Z. Chen, C. Yan, A. Selloni, C. G. Tully, X. Yang and B. E. Koel, Increasing Iridium Oxide Activity for the Oxygen Evolution Reaction with Hafnium Modification, *J. Am. Chem. Soc.*, 2021, **143**, 15616–15623.

26 W. Huo, X. Zhou, Y. Jin, C. Xie, S. Yang, J. Qian, D. Cai, Y. Ge, Y. Qu, H. Nie and Z. Yang, Rhenium Suppresses Iridium (IV) Oxide Crystallization and Enables Efficient, Stable Electrochemical Water Oxidation, *Small*, 2023, **19**, 2207847.

27 Z. L. Zhao, Q. Wang, X. Huang, Q. Feng, S. Gu, Z. Zhang, H. Xu, L. Zeng, M. Gu and H. Li, Boosting the oxygen evolution reaction using defect-rich ultra-thin ruthenium oxide nanosheets in acidic media, *Energy Environ. Sci.*, 2020, **13**, 5143–5151.

28 L. Cao, Q. Luo, J. Chen, L. Wang, Y. Lin, H. Wang, X. Liu, X. Shen, W. Zhang, W. Liu, Z. Qi, Z. Jiang, J. Yang and T. Yao, Dynamic oxygen adsorption on single-atomic Ruthenium catalyst with high performance for acidic oxygen evolution reaction, *Nat. Commun.*, 2019, **10**, 4849.

29 Y. Qiu, Y. Rao, Y. Zheng, H. Hu, W. Zhang and X. Guo, Activating ruthenium dioxide via compressive strain achieving efficient multifunctional electrocatalysis for Zn-air batteries and overall water splitting, *InfoMat*, 2022, **4**, e12326.

30 X. Miao, L. Zhang, L. Wu, Z. Hu, L. Shi and S. Zhou, Quadruple perovskite ruthenate as a highly efficient catalyst for acidic water oxidation, *Nat. Commun.*, 2019, **10**, 3809.

31 M. A. Hubert, A. M. Patel, A. Gallo, Y. Liu, E. Valle, M. Ben-Naim, J. Sanchez, D. Sokaras, R. Sinclair, J. K. Nørskov, L. A. King, M. Bajdich and T. F. Jaramillo, Acidic Oxygen Evolution Reaction Activity–Stability Relationships in Ru-Based Pyrochlores, *ACS Catal.*, 2020, **10**, 12182–12196.

32 Y. Chen, H. Li, J. Wang, Y. Du, S. Xi, Y. Sun, M. Sherburne, J. W. Ager, A. C. Fisher and Z. J. Xu, Exceptionally active iridium evolved from a pseudo-cubic perovskite for oxygen evolution in acid, *Nat. Commun.*, 2019, **10**, 572.

33 H. Liu, Z. Zhang, M. Li, Z. Wang, X. Zhang, T. Li, Y. Li, S. Tian, Y. Kuang and X. Sun, Iridium Doped Pyrochlore Ruthenates for Efficient and Durable Electrocatalytic Oxygen Evolution in Acidic Media, *Small*, 2022, **18**, 2202513.

34 S. Cherevko, A. R. Zeradjanin, A. A. Topalov, N. Kulyk, I. Katsounaros and K. J. J. Mayrhofer, Dissolution of Noble Metals during Oxygen Evolution in Acidic Media, *ChemCatChem*, 2014, **6**, 2219–2223.

35 K. Macounova, M. Makarova and P. Krtil, Oxygen evolution on nanocrystalline RuO2 and Ru0.9Ni0.1O2−δ electrodes – DEMS approach to reaction mechanism determination, *Electrochem. Commun.*, 2009, **11**, 1865–1868.

36 K. A. Stoerzinger, O. Diaz-Morales, M. Kolb, R. R. Rao, R. Frydendal, L. Qiao, X. R. Wang, N. B. Halck, J. Rossmeisl, H. A. Hansen, T. Vegge, I. E. L. Stephens, M. T. M. Koper and Y. Shao-Horn, Orientation-Dependent Oxygen Evolution on RuO_2 without Lattice Exchange, *ACS Energy Lett.*, 2017, **2**, 876–881.

37 O. Kasian, S. Geiger, T. Li, J.-P. Grote, K. Schweinar, S. Zhang, C. Scheu, D. Raabe, S. Cherevko, B. Gault and K. J. J. Mayrhofer, Degradation of iridium oxides via oxygen evolution from the lattice: correlating atomic scale structure with reaction mechanisms, *Energy Environ. Sci.*, 2019, **12**, 3548–3555.

38 S. B. Scott, J. E. Sørensen, R. R. Rao, C. Moon, J. Kibsgaard, Y. Shao-Horn and I. Chorkendorff, The low overpotential regime of acidic water oxidation part II: trends in metal and oxygen stability numbers, *Energy Environ. Sci.*, 2022, **15**, 1988–2001.

39 F. Hess, S. Rohrlack, M. Knapp and H. Over, Evidence of a Tetrahedrally Coordinated RuO_4 Surface Complex on RuO_2 (100): Density Functional Theory and Beyond, *J. Phys. Chem. C*, 2022, **126**, 946–956.

40 F. Hess and H. Over, Coordination Inversion of the Tetrahedrally Coordinated Ru_{4f} Surface Complex on RuO_2 (100) and Its Decisive Role in the Anodic Corrosion Process, *ACS Catal.*, 2023, **13**, 3433–3443.

41 K. Klyukin, A. Zagalskaya and V. Alexandrov, Role of Dissolution Intermediates in Promoting Oxygen Evolution Reaction at RuO_2 (110) Surface, *J. Phys. Chem. C*, 2019, **123**, 22151–22157.

42 A. Goryachev, M. Etzi Coller Pascuzzi, F. Carlà, T. Weber, H. Over, E. J. M. Hensen and J. P. Hofmann, Electrochemical stability of RuO_2(110)/Ru(0001) model electrodes in the oxygen and chlorine evolution reactions, *Electrochim. Acta*, 2020, **336**, 135713.

43 A. Zagalskaya and V. Alexandrov, Mechanistic Study of IrO_2 Dissolution during the Electrocatalytic Oxygen Evolution Reaction, *J. Phys. Chem. Lett.*, 2020, **11**, 2695–2700.

44 A. Lončar, D. Escalera-Lópe z, S. Cherevko and N. Hodnik, Inter-relationships between Oxygen Evolution and Iridium Dissolution Mechanisms, *Angew. Chem., Int. Ed.*, 2022, **61**, e202114437.

45 G. Kresse and J. Furthmüller, Efficiency of ab-initio total energy calculations for metals and semiconductors using a plane-wave basis set, *Comput. Mater. Sci.*, 1996, **6**, 15–50.

46 G. Kresse and J. Furthmüller, Efficient iterative schemes for ab initio total-energy calculations using a plane-wave basis set, *Phys. Rev. B: Condens. Matter Mater. Phys.*, 1996, **54**, 11169–11186.

47 P. E. Blöchl, Projector augmented-wave method, *Phys. Rev. B: Condens. Matter Mater. Phys.*, 1994, **50**, 17953–17979.

48 J. P. Perdew, K. Burke and M. Ernzerhof, Generalized Gradient Approximation Made Simple, *Phys. Rev. Lett.*, 1996, **77**, 3865–3868.

49 S. Grimme, J. Antony, S. Ehrlich and H. Krieg, A consistent and accurate ab initio parametrization of density functional dispersion correction (DFT-D) for the 94 elements H-Pu, *J. Chem. Phys.*, 2010, **132**, 154104.

50 S. Grimme, S. Ehrlich and L. Goerigk, Effect of the damping function in dispersion corrected density functional theory, *J. Comput. Chem.*, 2011, **32**, 1456–1465.

51 A. Zagalskaya and V. Alexandrov, Role of Defects in the Interplay between Adsorbate Evolving and Lattice Oxygen Mechanisms of the Oxygen Evolution Reaction in RuO_2 and IrO_2, *ACS Catal.*, 2020, **10**, 3650–3657.

52 Y. Ping, W. A. Goddard and G. A. Galli, Energetics and Solvation Effects at the Photoanode/Catalyst Interface: Ohmic Contact versus Schottky Barrier, *J. Am. Chem. Soc.*, 2015, **137**, 5264–5267.

53 R. R. Rao, M. J. Kolb, N. B. Halck, A. F. Pedersen, A. Mehta, H. You, K. A. Stoerzinger, Z. Feng, H. A. Hansen, H. Zhou, L. Giordano, J. Rossmeisl, T. Vegge, I. Chorkendorff, I. E. L. Stephens and Y. Shao-Horn, Towards identifying the active sites on RuO_2 (110) in catalyzing oxygen evolution, *Energy Environ. Sci.*, 2017, **10**, 2626–2637.

54 D. González, J. Heras-Domingo, S. Pantaleone, A. Rimola, L. Rodríguez-Santiago, X. Solans-Monfort and M. Sodupe,

Water Adsorption on MO_2 (M = Ti, Ru, and Ir) Surfaces. Importance of Octahedral Distortion and Cooperative Effects, *ACS Omega*, 2019, **4**, 2989–2999.

55 Q. Liang, A. Bieberle-Hütter and G. Brocks, Anti-Ferromagnetic RuO2: A Stable and Robust OER Catalyst over a Large Range of Surface Terminations, *J. Phys. Chem. C*, 2022, **126**, 1337–1345.

56 L. F. Mattheiss, Electronic structure of RuO_2, OsO_2, and IrO_2, *Phys. Rev. B*, 1976, **13**, 2433–2450.

57 J. Song, C. Wei, Z.-F. Huang, C. Liu, L. Zeng, X. Wang and Z. J. Xu, A review on fundamentals for designing oxygen evolution electrocatalysts, *Chem. Soc. Rev.*, 2020, **49**, 2196–2214.

58 A. Grimaud, O. Diaz-Morales, B. Han, W. T. Hong, Y.-L. Lee, L. Giordano, K. A. Stoerzinger, M. T. M. Koper and Y. Shao-Horn, Activating lattice oxygen redox reactions in metal oxides to catalyse oxygen evolution, *Nat. Chem.*, 2017, **9**, 457–465.

59 F. Song, M. M. Busch, B. Lassalle-Kaiser, C.-S. Hsu, E. Petkucheva, M. Bensimon, H. M. Chen, C. Corminboeuf and X. Hu, An Unconventional Iron Nickel Catalyst for the Oxygen Evolution Reaction, *ACS Cent. Sci.*, 2019, **5**, 558–568.

60 H. Jin, X. Liu, P. An, C. Tang, H. Yu, Q. Zhang, H.-J. Peng, L. Gu, Y. Zheng, T. Song, K. Davey, U. Paik, J. Dong and S.-Z. Qiao, Dynamic rhenium dopant boosts ruthenium oxide for durable oxygen evolution, *Nat. Commun.*, 2023, **14**, 354.

61 W. Huo, X. Zhou, Y. Jin, C. Xie, S. Yang, J. Qian, D. Cai, Y. Ge, Y. Qu, H. Nie and Z. Yang, Rhenium Suppresses Iridium (IV) Oxide Crystallization and Enables Efficient, Stable Electrochemical Water Oxidation, *Small*, 2023, **19**, 2207847.

62 Z.-Y. Wu, F.-Y. Chen, B. Li, S.-W. Yu, Y. Z. Finfrock, D. M. Meira, Q.-Q. Yan, P. Zhu, M.-X. Chen, T.-W. Song, Z. Yin, H.-W. Liang, S. Zhang, G. Wang and H. Wang, Non-iridium-based electrocatalyst for durable acidic oxygen evolution reaction in proton exchange membrane water electrolysis, *Nat. Mater.*, 2023, **22**, 100–108.

63 X. Wang, X. Wan, X. Qin, C. Chen, X. Qian, Y. Guo, Q. Xu, W.-B. Cai, H. Yang and K. Jiang, Electronic Structure Modulation of RuO_2 by TiO_2 Enriched with Oxygen Vacancies to Boost Acidic O_2 Evolution, *ACS Catal.*, 2022, **12**, 9437–9445.

64 L. Tian and C. Fei-Wu, Meaning and Functional Form of the Electron Localization Function, *Acta Phys.-Chim. Sin.*, 2011, **27**, 2786–2792.

65 A. D. Becke and K. E. Edgecombe, A simple measure of electron localization in atomic and molecular systems, *J. Chem. Phys.*, 1990, **92**, 5397–5403.

66 X. Zhang, H. Yin, C. Dang, H. Nie, Z. Huang, S. Zheng, M. Du, Z. Gu, J. Cao and X. Wu, Unlocking Enhanced Catalysis Stability in Acidic Oxygen Evolution: Structural Insights for PEM Applications under High-Current Density, *Angew. Chem., Int. Ed.*, 2025, e202425569.

67 Y. Wang, S. Hou, R. Ma, J. Jiang, Z. Shi, C. Liu, J. Ge and W. Xing, Modulating Crystallinity and Surface Electronic Structure of IrO_2 via Gadolinium Doping to Promote Acidic Oxygen Evolution, *ACS Sustainable Chem. Eng.*, 2021, **9**, 10710–10716.